Chemometrics and Intelligent Laboratory Systems 93 (2008) 120–131

Contents lists available at ScienceDirect

Chemometrics and Intelligent Laboratory Systems

journal homepage: www.elsevier.com/locate/chemolab

Uncertainties and error propagation in kinetic hard-modelling of spectroscopic data

Julien Billeter [a], Yorck-Michael Neuhold [a,*], Levente Simon [a], Graeme Puxty [b], Konrad Hungerbühler [a]

[a] Institute for Chemical and Bioengineering, Safety and Environmental Technology Group, ETH Zürich, 8093 Zürich, Switzerland
[b] CSIRO Energy Technology, PO Box 330, Newcastle NSW 2300, Australia

ARTICLE INFO

Article history:
Received 28 February 2008
Received in revised form 24 April 2008
Accepted 5 May 2008
Available online 11 May 2008

Keywords:
Kinetics
Hard-modelling
Error propagation
UV–vis spectroscopy
Mid-IR spectroscopy

ABSTRACT

A novel method is presented for the rigorous propagation of uncertainties in initial concentrations and in dosing rates into the errors in the rate constants fitted by multivariate kinetic hard-modelling of spectroscopic data using the Newton–Gauss–Levenberg/Marquardt optimisation algorithm. The method was successfully validated by Monte-Carlo sampling. The impact of the uncertainties in initial concentrations and in the dosing rate was quantified for simulated spectroscopic data based on a second and a formal third order rate law under batch and semi-batch conditions respectively. An important consequence of this study regarding optimum experimental design is the fact that the propagated error in a second order rate constant is minimal under exact stoichiometric conditions or when the reactant with the lowest associated uncertainty in its initial concentration is in a reasonable excess (pseudo first order conditions). As an experimental example, the reaction of benzophenone with phenylhydrazine in THF was investigated repeatedly (17 individual experiments) by UV–vis and mid-IR spectroscopy under the same semi-batch conditions, dosing the catalyst acetic acid. For all experiments and spectroscopic signals, reproducible formal third order rate constants were determined. Applying the proposed method of error propagation to any single experiment, it was possible to predict 80% (UV–vis) and 40% (mid-IR) of the observed standard deviation in the rate constants obtained from all experiments. The largest contribution to this predicted error in the rate constant could be assigned to the dosing rate. The proposed method of error propagation is flexible and can straightforwardly be extended to propagate other possible sources of error.

1. Introduction

It is a common trend in the chemical and pharmaceutical industry to maximise yield and safety while minimising the waste produced during manufacturing [1–3]. New processes need to be designed accordingly and existing ones may require re-evaluation of the process conditions in order to meet new standards [4].

There are various techniques in order to optimise a reaction process based on spectroscopic measurements. Soft-modelling methods such as principal component analysis [5], evolving factor analysis [6] and alternating least squares [7–10] have no or limited predictive capability. Predictive capability is possible for calibration methods [11] such as principal component regression [5], partial least squares [12] and neural networks [13]. However, these methods only allow for interpolation within the calibration set and are not suitable for extrapolation. The method used in this work, kinetic hard-modelling, does allow for both interpolation and extrapolation when an appropriate empirical or molecular rate law is applied reflecting the underlying reaction mechanism [14–19]. This task is facilitated by the recent development of multivariate analytical in-situ devices and optimisation algorithms [20,21].

For kinetic analysis via absorption spectroscopy (e.g. UV–vis and mid-IR), two classes of model parameters can be distinguished based on their relationship to the measured signal. Rate constants that define the kinetic model and thus the concentration profiles are nonlinear parameters with respect to the measured absorbance. According to Beer's law, molar component spectra are linear parameters that can be eliminated from the optimisation problem [14]. It is then the task of optimisation algorithms to minimise the difference between the experimental and modelled absorbance data. In recent years, the Newton–Gauss-Levenberg/Marquardt (NGL/M) algorithm that minimises this difference in the least squares sense has become the method of choice to solve such problems [14,19,22–25].

As a gradient method, the NGL/M algorithm directly allows estimation of the uncertainty in the fitted rate constants based on the corresponding variance/covariance matrix from one measurement only [24,25]. However, this calculation systematically underestimates this uncertainty when compared to the one resulting from multiple repetitions of the experiment under the same conditions.

Some other contributions to the uncertainty in the rate constants, such as baseline shifts [26,27], spectral constraints in the least squares [28] and preceding calibration procedures [29] have been studied.

* Corresponding author. Institute for Chemical and Bioengineering Safety and Environmental Technology Group, ETH Zürich, Hönggerberg HCI G130, 8093 Zürich, Switzerland. Tel.: +41 43 633 43 73; fax: +41 43 632 11 89.
E-mail address: bobby.neuhold@chem.ethz.ch (Y.-M. Neuhold).

0169-7439/$ – see front matter © 2008 Elsevier B.V. All rights reserved.
doi:10.1016/j.chemolab.2008.05.001

Also, bootstrapping has been compared to variance-covariance based uncertainty calculations [30]. However, under strictly controlled isothermal conditions, and provided the kinetic model is correct, uncertainties in the initial concentrations and/or dosing rates (semi-batch) are also likely to represent major contributing factors. To our knowledge, these uncertainties have not yet been incorporated into a kinetic hard-modelling procedure.

In the present article, the impact of these additional uncertainties is investigated and quantified by classical error propagation. In this context, based on some selected kinetic mechanisms, simulated spectroscopic data are analysed under batch or semi-batch conditions by the NGL/M algorithm combined with error propagation. This method was also applied to the reaction of benzophenone with phenylhydrazine [31] and the predicted error in the rate constant was compared to the uncertainty obtained from multiple experimental repetitions. The reaction was followed by UV–vis and mid-IR spectroscopy under strictly isothermal semi-batch conditions.

2. Theoretical considerations

Kinetic modelling applied to spectroscopy relies on Beer's law to decompose a measured signal into the concentration and the molar spectra of the pure components. Beer's law can be written elegantly in matrix notation.

$$\mathbf{Y} = \mathbf{CA} + \mathbf{R} \tag{1}$$

where $\mathbf{Y}$ ($nt \times nw$) represents the spectroscopic measurements, i.e. the time and wavelength/wavenumber resolved absorbance signals, $\mathbf{C}$ ($nt \times nc$) the concentration profiles of the contributing species and $\mathbf{A}$ ($nc \times nw$) the pure component spectra, i.e. the molar absorptivities multiplied by the path length. Here, nt is the number of reaction times, nw the number of wavelengths/wavenumbers and nc the number of absorbing species. The residual matrix $\mathbf{R}$ ($nt \times nw$) comprises the deviation from Beer's law due to inherent experimental noise. It is assumed that the baseline does not change with time. For details on the notation, we refer to Section 6.

The matrix of concentration profiles $\mathbf{C}$ are calculated by numerical integration of the system of ordinary differential equations describing the kinetic 'hard' model by elementary steps of the corresponding chemical equations [17,32]. Note that $\mathbf{C}$ is a function of the selected model, the rate constants $\mathbf{k}$ ($1 \times nk$), the initial concentrations $\mathbf{c_0}$ ($1 \times nc$) and the dosing (flow) rate $\mathbf{f}$ ($1 \times nf$); nk denotes the number of chemical rate constants, nf is the number of different dosing steps. In kinetic hard-modelling, $\mathbf{c_0}$ and $\mathbf{f}$ are treated as known *a priori* information and generally not fitted.

$$\mathbf{R}(\text{model}, \mathbf{k}, \mathbf{c}_0, \mathbf{f}) = \mathbf{Y} - \mathbf{C}(\textit{model}, \mathbf{k}, \mathbf{c}_0, \mathbf{f})\mathbf{A} \tag{2}$$

In least-squares analysis, the sum of squares, ssq, is calculated from the residuals $\mathbf{R}$ and used as the objective function to be minimised by iteratively changing $\mathbf{k}$. The gradient-based Newton–Gauss–Levenberg/Marquardt algorithm (NGL/M) [14,19,22–25] is used to solve this nonlinear regression.

$$ssq = \sum_{i=1}^{nt}\sum_{j=1}^{nw} r_{i,j}^2 \tag{3}$$

Note that $\mathbf{A}$ is comprised by linear parameters only and can be eliminated from the nonlinear optimisation by its linear least-squares estimate according to Eq. 4 [14].

$$\mathbf{A} = \mathbf{C}^{+}\mathbf{Y} = \left(\mathbf{C}^{\mathrm{T}}\mathbf{C}\right)^{-1}\mathbf{C}^{\mathrm{T}}\mathbf{Y} \tag{4}$$

where $\mathbf{C}^{+}$ denotes the pseudo-inverse of $\mathbf{C}$. Importantly, baseline variations along the wavelengths/wavenumbers have no impact on the least squares minimum, they only affect the fitted pure component spectra $\mathbf{A}$.

Any gradient-based optimisation method requires the calculation of a Jacobian, i.e. the first partial derivative of the residuals $\mathbf{R}$ with respect to $\mathbf{k}$. As this would lead to a three dimensional Jacobian, it is convenient to unfold $\mathbf{R}$ into a long vector $\mathbf{r}$ ($nt \cdot nw \times 1$) [18]. Then, the Jacobian $\mathbf{J}$ ($nt \cdot nw \times nk$) can be calculated by a forward finite difference, as illustrated by Eq. 5.

$$\mathbf{J} = \left(\frac{\partial \mathbf{r}}{\partial \mathbf{k}}\right) = \left[\left(\frac{\partial \mathbf{r}}{\partial k_1}\right)\left(\frac{\partial \mathbf{r}}{\partial k_2}\right)\cdots\left(\frac{\partial \mathbf{r}}{\partial k_{nk}}\right)\right] \text{with} \left(\frac{\partial \mathbf{r}}{\partial k_i}\right) \approx \frac{\mathbf{r}(\mathbf{k} + \delta k_i) - \mathbf{r}(\mathbf{k})}{\delta k_i} \tag{5}$$

where k_i is the i-th rate constant and δk_i the finite difference applied to the i-th rate constant.

The Jacobian is used by the NGL/M algorithm to iteratively shift $\mathbf{k}$ towards an optimum. For details see [17]. $\mathbf{J}$ is also used to approximate the Hessian $\mathbf{H}(nk \times nk) \approx \mathbf{J}^{\mathbf{T}}\mathbf{J}$ [19]. Based on the inverted Hessian $\mathbf{H}^{-1}$, the variance $\sigma_{k_i}^2$ associated with the i-th rate constant can be estimated from the variance/covariance matrix.

$$\sigma_{k_i}^2 = d_{i,i}\sigma_{\mathbf{r}}^2 \tag{6}$$

where $d_{i,i}$ denotes the i-th diagonal element of the inverted Hessian $\mathbf{H}^{-1}$. The scalar σ_{r}^2, the variance of the residuals, is an estimate of the 'true' variance σ_y^2 in the measurement matrix $\mathbf{Y}$, provided the noise is normally distributed and homoscedastic. It can be calculated from

$$\sigma_r^2 = \frac{ssq}{nt \cdot nw - (nk + nc \cdot nw)} \approx \sigma_{\mathrm{y}}^2 \tag{7}$$

The denominator of this equation represents the degrees of freedom, i.e. the number of experimental data points ($nt \cdot nw$) minus the number of fitted rate constants (nk) and fitted molar spectra of all absorbing species ($nc \cdot nw$).

Eq. 6 can be written in convenient matrix notation.

$$\boldsymbol{\sigma}_{\mathbf{k}}^2 = \mathrm{diag}\left(\mathbf{H}^{-1}\right)\sigma_{\mathbf{r}}^2 \tag{8}$$

Note that in analogy to Matlab [33], the 'diag' operator extracts a vector of diagonal elements from the corresponding matrix.

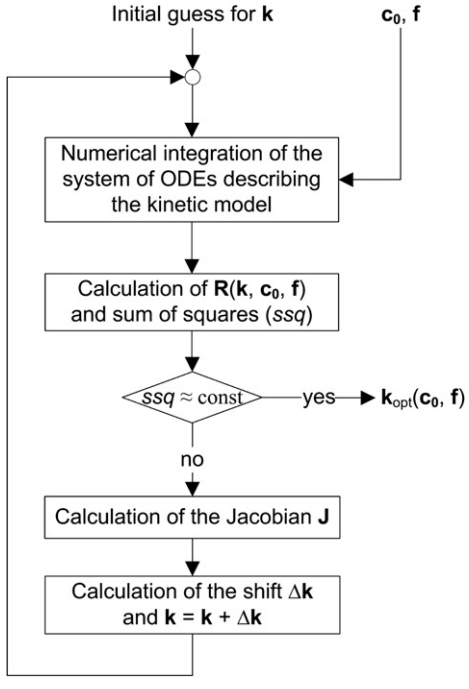

Fig. 1. Simplified scheme of the NGL/M algorithm used in kinetic hard-modelling.

The iterative process performed by the NGL/M algorithm in order to optimise the vector of rate constants **k** is outlined in Fig. 1.

The vector of variances, $\boldsymbol{\sigma}^2_{\mathbf{k}}$, calculated by Eq. 8, only covers the variances due to the residuals and the sensitivities of the rate constants with respect to these residuals. However, other additional sources of error are inherently present. Amongst these, the uncertainties in the initial concentrations and in the dosing rates are likely to have a significant impact on the variances of the calculated rate constants, provided the temperature is constant during the reaction and its fluctuation can be neglected. Eqs. 6 and 8 can be adapted to consider these additional uncertainties by classical error propagation [34].

$$\sigma^2_{k_i} = d_{i,i}\sigma^2_{\mathbf{r}} + \sum_{n=1}^{nc}\left(\frac{\partial k_i}{\partial c_{0,n}}\right)^2\sigma^2_{c_{0,n}} + \sum_{m=1}^{nf}\left(\frac{\partial k_i}{\partial f_m}\right)^2\sigma^2_{f_m} \tag{9}$$

or in matrix notation:

$$\boldsymbol{\sigma}^2_{\mathbf{k}} = \underbrace{\mathrm{diag}\left(\mathbf{H}^{-1}\right)\sigma^2_{\mathbf{r}}}_{=\boldsymbol{\sigma}^2_{\mathbf{k},\mathbf{r}}} + \underbrace{\mathrm{diag}\left(\left(\frac{\partial \mathbf{k}}{\partial \mathbf{c}_0}\right)^{\mathrm{T}}\mathrm{DIAG}\left(\boldsymbol{\sigma}^2_{\mathbf{c}_0}\right)\left(\frac{\partial \mathbf{k}}{\partial \mathbf{c}_0}\right)\right)}_{=\boldsymbol{\sigma}^2_{\mathbf{k},\mathbf{c}_0}} + \underbrace{\mathrm{diag}\left(\left(\frac{\partial \mathbf{k}}{\partial \mathbf{f}}\right)^{\mathrm{T}}\mathrm{DIAG}\left(\sigma^2_{\mathbf{f}}\right)\left(\frac{\partial \mathbf{k}}{\partial \mathbf{f}}\right)\right)}_{=\boldsymbol{\sigma}^2_{\mathbf{k},\mathbf{f}}} \tag{10}$$

In Eq. 10, vectors $\boldsymbol{\sigma}^2_{\mathbf{c}_0}$ and $\boldsymbol{\sigma}^2_{\mathbf{f}}$ contain the variances corresponding to the initial concentrations $\mathbf{c_0}$ and to the dosing rates **f**. The partial derivatives $\partial\mathbf{k}/\partial\mathbf{c}_0$ and $\partial\mathbf{k}/\partial\mathbf{f}$ comprise the sensitivities of the rate constants with respect to the initial concentrations and with respect to the dosing rates. Throughout this manuscript, we will refer to the first term of Eq. 10 as the variance of **k** due to the residuals, $\boldsymbol{\sigma}^2_{\mathbf{k},\mathbf{r}}$, to the second term as the variance due to the initial concentrations, $\boldsymbol{\sigma}^2_{\mathbf{k},\mathbf{c}_0}$, and to the last term as the variance due to the dosing rates, $\boldsymbol{\sigma}^2_{\mathbf{k},\mathbf{f}}$. Note that the upper case 'DIAG' operator generates a diagonal matrix from the corresponding vector argument and thus performs the reverse operation compared to the lower case 'diag' operator introduced previously.

The sensitivity factors $\partial\mathbf{k}/\partial\mathbf{c}_0$ and $\partial\mathbf{k}/\partial\mathbf{f}$ were evaluated numerically and estimated by the method of central finite differences. The use of this method, as opposed to the forward finite difference, was required to improve the numerical stability of the derivatives.

$$\left(\frac{\partial \mathbf{k}}{\partial c_{0,n}}\right) \approx \frac{\mathbf{k}_{\mathrm{opt}}\left(\mathbf{c}_0 + \delta c_{0,n}, \mathbf{f}\right) - \mathbf{k}_{\mathrm{opt}}\left(\mathbf{c}_0 - \delta c_{0,n}, \mathbf{f}\right)}{2\delta c_{0,n}} \tag{11}$$

$$\left(\frac{\partial \mathbf{k}}{\partial f_m}\right) \approx \frac{\mathbf{k}_{\mathrm{opt}}\left(\mathbf{c}_0, \mathbf{f} + \delta f_m\right) - \mathbf{k}_{\mathrm{opt}}\left(\mathbf{c}_0, f - \delta f_m\right)}{2\delta f_m}. \tag{12}$$

The finite differences $\delta c_{0,n}$ and δf_m used to calculate the derivatives were set to 0.1% of the corresponding values $c_{0,n}$ and f_m. This

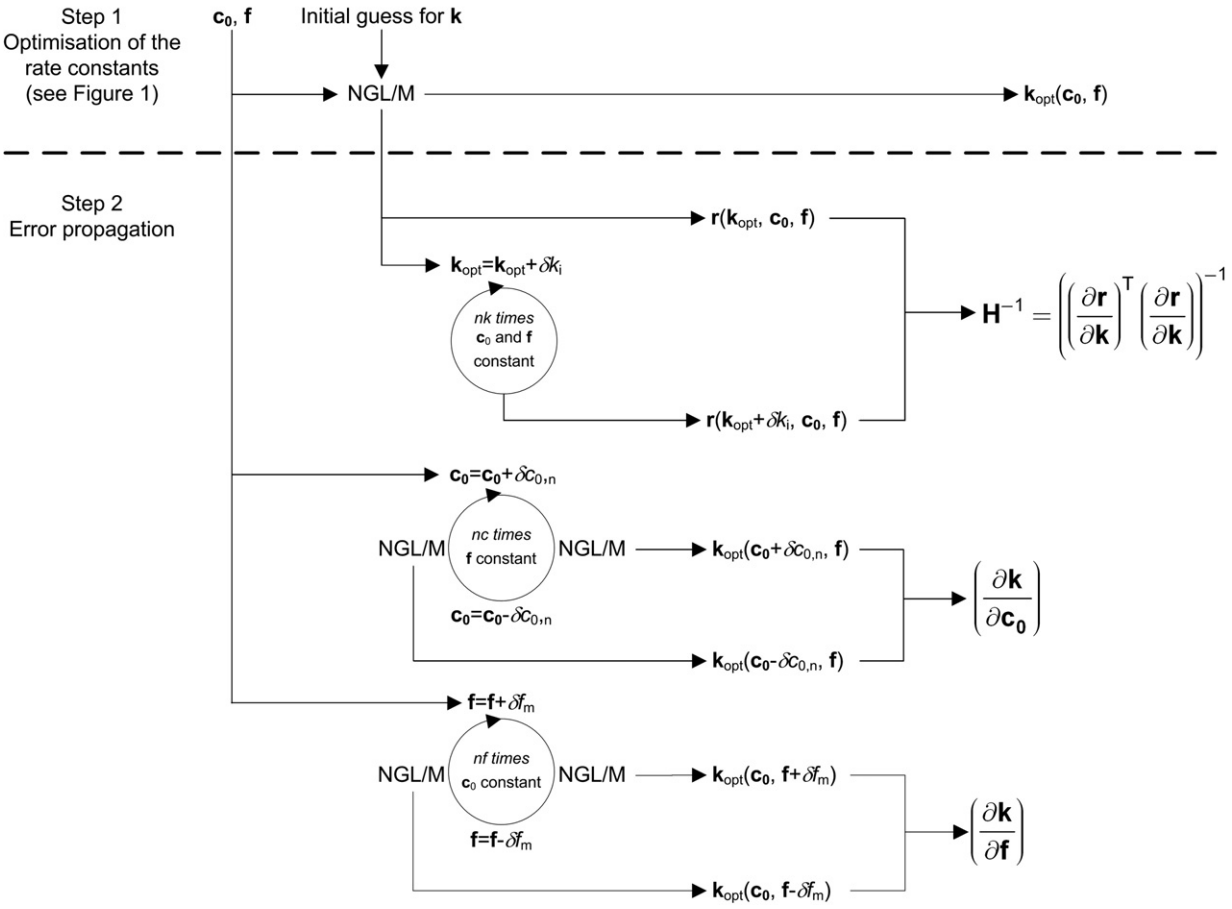

Fig. 2. Simplified scheme to determine the inverted Hessian $\mathbf{H}^{-1}$ and the derivatives ($\partial\mathbf{k}/\partial\mathbf{c}_0$) and ($\partial\mathbf{k}/\partial\mathbf{f}$) calculated by the NGL/M algorithm.

Table 1
List of the mechanisms used to generate simulated data

Mechanism	Rate law[a]	k[b]	Order	Dosing	Section
$A+B\rightarrow P$ or S[c]	$dc_{t,P}/dt=dc_{t,S}/dt=k\cdot c_{t,A}c_{t,B}$	0.5	2	No	4.1.1
$A+B+C\rightarrow P+C$ with C as catalyst	$dc_{t,P}/dt = k\cdot c_{t,A}c_{t,B}c_{t,C}-\frac{1}{V_t}\left(\frac{dV_t}{dt}\right)c_{t,P}$ $dc_{t,C}/dt = \frac{1}{V_t}\left(\frac{dV_t}{dt}\right)(c_{\mathrm{dos},C}-c_{t,C})$[d]	$1.75\cdot10^{-4}$	3[e]	Yes	4.1.2

[a] The remaining derivatives can be calculated by closure.
[b] $[\mathrm{LmoL^{-1}s^{-1}}]$ for 2nd and $[\mathrm{L^2mol^{-2}s^{-1}}]$ for 3rd order rate constants.
[c] Pure component spectra of P and S were generated to produce different overlaps with A and B (see Fig. 3).
[d] The change of volume per unit of time, dV_t/dt, is the flow rate f associated with the dosing event for species C of dosed catalyst concentration $c_{\mathrm{dos},C}$.
[e] Observed order due to a steady state assumption (see Section 4.1.2 for details).

ensured the numerical stability for all examples presented in this article. $\mathbf{k}_{\mathrm{opt}}$ refers to the calculated optimum rate constants that minimise the residuals in the least-squares sense. For each finite difference by which an initial concentration or the dosing rate is modified, $\mathbf{k}_{\mathrm{opt}}$ has to be re-determined by the NGL/M algorithm. The whole procedure is presented in Fig. 2.

As indicated by Figs. 1 and 2, error propagation problems of this kind cannot be solved explicitly. This is due to the fact that outer nonlinear regression coupled to the inner nested integration of rate laws has no explicit solution except for some rare cases. Therefore an iterative computation is required.

3. Simulations and experiments

3.1. Simulations

Additional contributions to the variance in the rate constant according to Eq. 10 are first investigated with simulated mechanisms. The simulated kinetic schemes considered here are summarised in Table 1.

Note that we defer from an investigation of zero and first order mechanisms. Formally, zero order kinetics depend on the initial concentration. However, as the rate is constant, the rate constant is linear with respect to the concentration profiles **C**. Thus it cannot be distinguished (and separated) from the molar spectra (that are also linear with **C**) within the fitting process without a priori knowledge on the pure component spectrum of the product. Incorporating a pure spectrum into the NGL/M fitting would require the propagation of its associated uncertainty. This was beyond the scope of this article. Naturally, first order kinetics are independent from initial concentrations, i.e. the optimum of the NGL/M fitting is invariant to their change. Therefore there is no associated error propagation for first order rate constants.

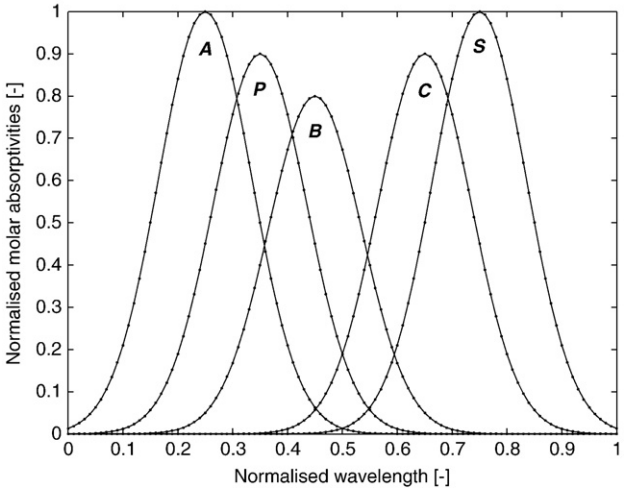

Fig. 3. Pure component spectra as a function of wavelength. The spectra were generated using Gaussian functions centred at 0.25 (species A), 0.35 (P), 0.45 (B), 0.65 (C), 0.75 (S) with a constant half width of 0.2. Species names correspond to the models given in Table 1. For the sake of simplicity, component spectra are set to a maximum of one and wavelengths are evenly distributed between 0 and 1.

Simulations were performed using Matlab [33]. Based on the selected molecular mechanism, the initial concentrations and the specified dosing rate, the corresponding system of differential equations was integrated by a 4th order Runge–Kutta method (Matlab's ode45 solver) resulting in the concentration profiles **C** for the individual species. Pure component spectra **A** were generated using Gaussian functions, displayed in Fig. 3. According to Eq. 1, spectroscopic absorbance data **Y** were generated by multiplication of **C** and **A**. Normally distributed noise with a constant absolute standard deviation $\sigma_{\mathbf{y}}=10^{-4}$ was added, accounting for 0.01–0.02% relative to the maximum absorbance of the corresponding **Y**.

For the second order mechanism in Table 1, data were simulated for ten thousand data points up to an end time representing 95% conversion. The third order model was chosen to correspond to the mechanism, time range, initial conditions, dosing rate and associated uncertainties that were the basis for the analysis of the experimental data. The mean optimum rate constant as determined from the fitting of all experimental data (see 3.2) was used for the simulation ($1.75\cdot10^{-4}\,\mathrm{L^2mol^{-2}s^{-1}}$). Pure component spectra were used according to Fig. 3.

Using the third order model, the validation of the proposed method for error propagation was done by Monte-Carlo sampling. For this, a set of 10^4 normally distributed initial concentrations and dosing rates was generated. The means were chosen to be the same as the experimental initial concentrations and dosing rate; the associated standard deviations were taken from a preceding error estimation covering the experimental preparation procedure (see 3.2 and Appendix). For each of the Monte-Carlo samples the rate constant was re-optimised. The standard deviation of these 10^4 calculated rate constants was then compared to its prediction from the propagation of the error in the mean initial concentrations and dosing rate.

3.2. Experiments

The reaction of benzophenone with phenylhydrazine under acidic excess can be followed both in the mid-IR and UV–vis spectral range [31]. The reaction scheme is given in Fig. 4.

3.2.1. Sample preparation

Seventeen solutions of benzophenone (Fluka purum, certified 99.9%) in THF (Across Organics for analysis) were prepared

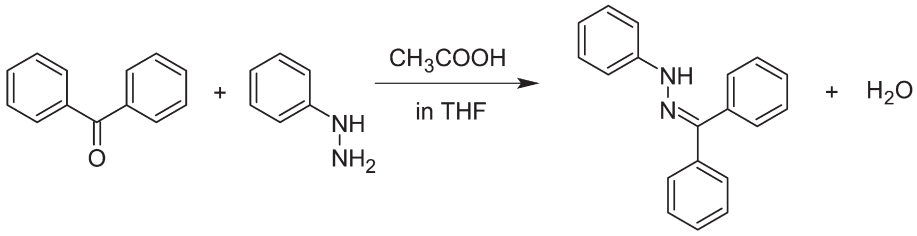

Fig. 4. Reaction between benzophenone and phenylhydrazine catalysed by acetic acid to form benzophenone phenylhydrazone and water.

independently by weighing between 7.3022 g and 7.3027 g of benzophenone into a volumetric flask and making up to 50 mL with THF. Phenylhydrazine (Aldrich-Fine Chemicals, certified 99.6%) solutions were prepared by weighing between 13.0004 g and 13.0010 g of phenylhydrazine into a 50 mL flask and making up to 50 mL with THF. At the start, the reactor vessel was charged with 15 mL of each solution and thermostated at 25 °C. This resulted in initial concentrations between 0.40033 $molL^{-1}$ and 0.40036 $molL^{-1}$ of benzophenone, and between 1.19737 $molL^{-1}$ and 1.19743 $molL^{-1}$ of phenylhydrazine. Note that for calculation of all concentrations, manufacturer's specifications for the purity were considered.

Error estimation in these initial concentrations due to sample preparation was performed by considering the following factors: standard deviation due to weighing (±0.0001 g), due to filling the volumetric flasks (±0.06 mL), and due to pipetting (±0.04 mL/pipette). For details, see Appendix. As the differences in weighed samples are very small, the impact of weighing is negligible compared to filling the flask and pipetting. This leads to one common set of initial concentrations with an associated uncertainty of 0.292% for both compounds and all 17 experiments. Note that manufacturer's uncertainties in the stated purity of the reactants were not available and so were not propagated through the sample preparation.

Initially, the dosing pump was calibrated at 8.17 $mLmin^{-1}$ by repeatedly weighing delivered volumes of water at 25 °C. The corresponding standard deviation (0.14 $mLmin^{-1}$) was close to the manufacturer's specification (0.2 $mLmin^{-1}$). For the dosed catalyst, glacial acetic acid, only an error in the dosing rate was considered as it was used directly from the bottle and there was no sample preparation procedure involved. For each experiment, the pump was filled at room temperature with 17.48376 $molL^{-1}$ glacial acetic acid (Carlo Erba Reagents for analysis, certified 100.0%). To initiate the reaction, 4.91 mL of the acid were dosed into the reactor content within 36 s. During the dosing period, a maximum temperature change of 0.5 °C was observed.

Any potential volume expansion or contraction due to the mixing of the reactant solutions was tested by the addition of appropriate volumes of all three compounds into a graduated cylinder. No deviation from volume additivity (15+15+5=35 mL) was detected during the course of the reaction within the scale of the cylinder (0.25 mL) or the overall uncertainty due to pipetting (±0.20 mL).

3.2.2. Instrumentation

Experiments were carried out in the Combined Reaction Calorimeter (CRC.v4) [35], a small-scale reaction calorimeter that combines the principle of power compensation and heat balance. It allows a maximum volume of 50 mL. Dosing was done by a Jasco HPLC pump (model PU-1580). Power compensation of the CRC.v4 is achieved by means of a compensation heater made of Hastelloy immersed into the reaction solution. The sensitivity of this compensation heater allows this calorimeter to maintain highly isothermal conditions (±0.04 °C), a prerequisite in order to minimise temperature effects on the error propagation. The jacket temperature is kept constant by Peltier elements. For a detailed description of the reactor, refer to [35].

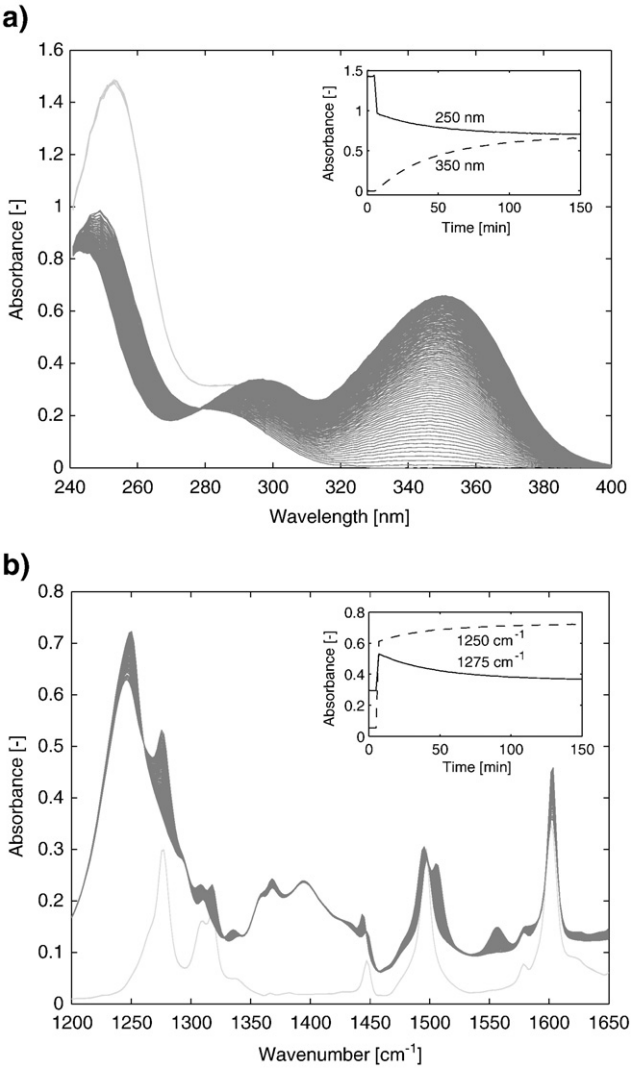

Fig. 5. Time resolved UV–vis (a) and mid-IR (b) absorbance spectra before dosing (light gray curves) and after dosing (dark gray curves) with corresponding kinetic traces as insets. The sudden changes in absorbance in the mid-IR region are due to dilution and absorption from dosing of the catalyst acetic acid. In the UV–vis region only dilution effects are observed during dosing.

Mid-IR signals were monitored between 1200 and 1650 cm^{-1} at 4 cm^{-1} resolution by Mettler Toledo's ReactIR 4000 system comprised of an FT-IR spectrometer connected via a K4 conduit to an ATR-IR crystal directly built into the bottom of the reactor vessel. UV–vis signals were followed between 240 and 400 nm at 1 nm resolution by a Cary 50 UV–vis spectrometer (Varian) coupled to a Hellma ATR-UV dip probe (model 661.804) immersed into the reactor. UV–vis and mid-IR signals were recorded simultaneously every minute for a total of 150 min. Fig. 5 shows a representative example of absorbance spectra acquired in the UV–vis and mid-IR range (solvent THF as reference background). No measurements were taken during the dosing period of 36 s.

4. Results and discussion

In the theoretical section, equations for error propagation were derived in a general way, i.e. covering multi step mechanisms and multiple dosing events. This required the use of a vector **k** for the rate constants and a vector **f** for the flow rates. As examples discussed in this section only comprise one step reactions and one dosing event, vectors **k** and **f** collapse to scalars. However, for the sake of simplicity, the vector notation (boldface lowercase) is maintained. Thus, these vectors and their corresponding variances contain one element only.

4.1. Simulated data

4.1.1. Second order model ($A+B \rightarrow P$ or S)

Second order reactions are amongst the most common reactions (although often simplified to pseudo-first order for mathematical ease). In the following, we investigate in detail the individual contributions of Eqs. 9 or 10 that lead to a propagated error in a second order rate constant. Batch conditions were considered (no dosing), so there is no uncertainty to be propagated that corresponds to a dosing rate and the third term of Eq. 10 can be disregarded. Thus, the variance of the second order rate constant $\boldsymbol{\sigma}^2_{\mathbf{k}}$ is the sum of the variance due to the residuals $\boldsymbol{\sigma}^2_{\mathbf{k},\mathbf{r}}$ and the variance due to the initial concentrations $\boldsymbol{\sigma}^2_{\mathbf{k},\mathbf{c}_0}$.

To study the impact of these individual contributions to the variance of the fitted rate constant, the ratio of the initial concentrations of reactants A and B was varied between 0.01 and 100 while keeping the sum of the initial concentrations of the two reactants, $c_{tot}=c_{0,A}+c_{0,B}$, constant at 1 $molL^{-1}$. Data with strongly overlapped simulated component spectra were used here (product P, see Table 1 and Fig. 3). As can be seen in Fig. 6, the variance $\boldsymbol{\sigma}^2_{\mathbf{k}}$ is dominated by $\boldsymbol{\sigma}^2_{\mathbf{k},\mathbf{c}_0}$, and $\boldsymbol{\sigma}^2_{\mathbf{k},\mathbf{r}}$ only plays a minor role at the chosen noise level of the simulated data ($\sigma_y=10^{-4}$). Both $\boldsymbol{\sigma}^2_{\mathbf{k},\mathbf{c}_0}$ as well as $\boldsymbol{\sigma}^2_{\mathbf{k}}$ show a sharp minimum at stoichiometric conditions ($c_{0,A}/c_{0,B}=1$). Slight deviations from stoichiometric conditions lead to an increase in $\boldsymbol{\sigma}^2_{\mathbf{k}}$ (and $\boldsymbol{\sigma}^2_{\mathbf{k},\mathbf{c}_0}$) whereas larger deviations (i.e. when moving towards pseudo-first order conditions) to a subsequent decrease.

However, in very large excess of either species (strong pseudo-first order conditions), $\boldsymbol{\sigma}^2_{\mathbf{k},\mathbf{r}}$ becomes more and more prominent and significantly adds to the total variance $\boldsymbol{\sigma}^2_{\mathbf{k}}$. This is due to the fact that the concentration of the limiting species is gradually decreasing as is the change in the absorbance. Eventually, it will reach the detection limit and no kinetics can be observed within the noise level of the instrument ($\sigma_r \approx \sigma_y$).

Note that a significant increase in the noise level σ_y of the simulated data matrix **Y** increases the contribution of $\boldsymbol{\sigma}^2_{\mathbf{k},\mathbf{r}}$ on $\boldsymbol{\sigma}^2_{\mathbf{k}}$ and distorts the characteristic shape of $\boldsymbol{\sigma}^2_{\mathbf{k},\mathbf{c}_0}$ shown in Fig. 6 no longer allowing for an interpretation. However, within one or two orders of magnitude in the noise level, $\boldsymbol{\sigma}^2_{\mathbf{k},\mathbf{c}_0}$ is hardly affected.

For further interpretation of the variance due to the initial concentrations (see Fig. 6), the factors contributing to $\boldsymbol{\sigma}^2_{\mathbf{k},\mathbf{c}_0}$ are investigated separately. According to Eq. 10, the variances in the initial concentrations $\boldsymbol{\sigma}^2_{\mathbf{c}_0}$ estimated by the experimenter weight the partial derivatives of **k** with respect to these initial concentrations. For this particular example, the variance $\boldsymbol{\sigma}^2_{\mathbf{k},\mathbf{c}_0}$ is $(\partial\mathbf{k}/\partial c_{0,A})^2 \cdot \sigma^2_{c_{0,A}} + (\partial\mathbf{k}/\partial c_{0,B})^2 \cdot \sigma^2_{c_{0,B}}$. Fig. 7a shows that the vector $\boldsymbol{\sigma}^2_{\mathbf{c}_0}=[\sigma^2_{c_{0,A}}, \sigma^2_{c_{0,B}}]$ is responsible for the asymmetry of $\boldsymbol{\sigma}^2_{\mathbf{k},\mathbf{c}_0}$ in Fig. 6, reflecting the difference in the relative errors imposed on the initial concentrations. Minima and maxima in $\boldsymbol{\sigma}^2_{\mathbf{k},\mathbf{c}_0}$ are due to the derivatives and their interpretation or prediction is difficult as they are the result of two preceding optimisations (NGL/M) required for the numerical differentiation (see Fig. 2).

A dramatic decrease of the spectral overlap (product P replaced by S, see Fig. 3) does not result in any observable effect on the squared derivatives of Fig. 7b and thus was not further investigated. However, a limited investigation on the effect of rate constant, conversion and sum of the initial concentrations on $\boldsymbol{\sigma}^2_{\mathbf{k},\mathbf{c}_0}$ revealed an impact on the squared derivatives $(\partial\mathbf{k}/\partial\mathbf{c}_{0,A})^2$ and $(\partial\mathbf{k}/\partial\mathbf{c}_{0,B})^2$. From an alternating variation of these parameters, the three following observations were made: (a) an increase of the rate constant narrows the minima and maxima of $\boldsymbol{\sigma}^2_{\mathbf{k},\mathbf{c}_0}$ in Fig. 6 and increases the derivatives; (b) with an increasing sum of the initial concentrations of the two reactants the derivatives also increase but their shape remains invariant; (c) both shape and magnitude of the derivatives are influenced by the conversion. The greater the conversion, the narrower becomes the minimum and the greater are the derivatives.

Nonlinear optimisation problems generally do not have explicit solutions. Therefore it is impossible to predict $\partial\mathbf{k}/\partial\mathbf{c}_0$ without the numerical solution of the NGL/M algorithm. However, second order rate laws can be integrated explicitly and may be used to estimate some boundaries for these derivatives. In order to test this, the concentration profiles resulting from the explicit integration [36] of the corresponding differential equations (see Table 1) were rearranged for **k** and then derived analytically with respect to the initial concentrations (see Appendix). These obtained predicted derivatives do not reflect the impact of fitting the absorbance data, i.e. they do not depend on **Y**, and are only a function of the rate law and the corresponding set of ordinary differential equations. Surprisingly, the analytical squared derivatives of **k** with respect to the species in excess approximate the

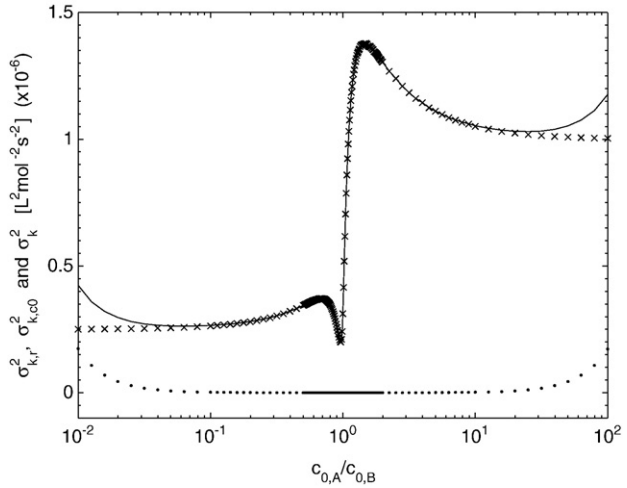

Fig. 6. Individual contributions $\boldsymbol{\sigma}^2_{\mathbf{k},\mathbf{r}}$ (dotted line) and $\boldsymbol{\sigma}^2_{\mathbf{k},\mathbf{c}_0}$ (crossed line) to the variance $\boldsymbol{\sigma}^2_{\mathbf{k}}$ (full line) of the fitted rate constant **k** as calculated from Eq. 10 for the second order model $A+B \rightarrow P$ at various ratios $c_{0,A}/c_{0,B}$ of the initial concentrations ($c_{0,A}+c_{0,B}=1$ $molL^{-1}$) and imposed uncertainties of $\sigma_{c_{0,A}}=0.2\%\ c_{0,A}$ and $\sigma_{c_{0,B}}=0.1\%\ c_{0,B}$.

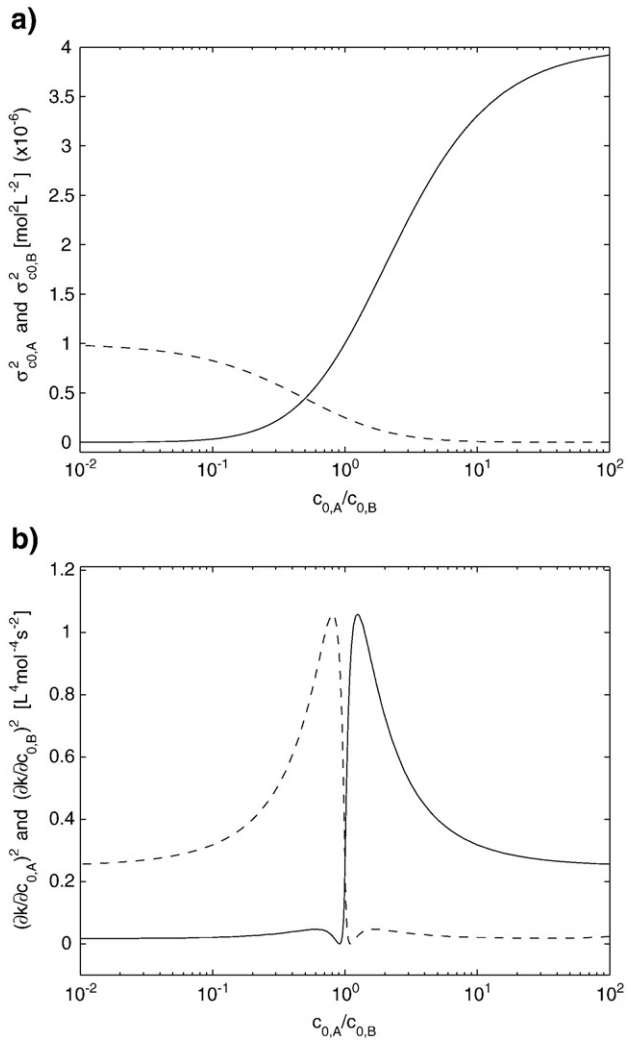

Fig. 7. (a) Squared estimated uncertainties $\boldsymbol{\sigma}^2_{\mathbf{c}_0}$ (full line $\boldsymbol{\sigma}^2_{\mathbf{c}_{0,A}}$, dashed line $\boldsymbol{\sigma}^2_{\mathbf{c}_{0,B}}$) in the initial concentrations and (b) squared derivatives of the fitted rate constant k with respect to the initial concentrations (full line $(\partial\mathbf{k}/\partial\mathbf{c}_{0,A})^2$, dashed line $(\partial\mathbf{k}/\partial\mathbf{c}_{0,B})^2$) for the second order model $A+B\rightarrow P$ at various ratios $c_{0,A}/c_{0,B}$ and for $c_{0,A}+c_{0,B}$=1 molL^{-1}.

ones from the fitting towards strong pseudo-first order conditions (far right or far left of Fig. 7b). In such conditions, the squared derivatives of $\mathbf{k}$ with respect to the limiting species and to the species in excess tend to zero and to $(\mathbf{k}/c_{\text{tot}})^2$ respectively. These limits coincide with the analytical solution presented in the Appendix. This is also the case at the stoichiometric ratio ($c_{0,A}/c_{0,B}$=1) where the squared derivatives from the fitting can again be predicted by their analytical solution, i.e. $(\mathbf{k}/c_{\text{tot}})^2$ for A and B (see Fig. 7b).

Despite these limits, it is not possible to approximate $\partial\mathbf{k}/\partial\mathbf{c}_0$ by an analytical equation due to an unpredictable impact of the nonlinear fitting. In particular, the analytical derivation from the rate law requires breaking the continuity of the derivatives towards stoichiometric conditions, i.e. there are two different explicit functions that define the squared derivatives at stoichiometric ($c_{0,A}=c_{0,B}$) and nonstoichiometric ($c_{0,A}\neq c_{0,B}$) conditions. As the analytical squared derivatives with respect to the species in excess tend towards infinity approaching stoichiometric conditions, the two maxima close to the stoichiometric point of Fig. 7b can be attributed to the fitting.

Figs. 6 and 7b suggest optimum experimental conditions when the two reactants are mixed in stoichiometric ratio. At this ratio, the impact of the errors in the initial concentrations on $\mathbf{k}$ is at its minimum. However, due to the fairly steep increase in the vicinity of the stoichiometric ratio (depending on the magnitude of the rate constant, the total concentration and conversion, as discussed above), it is preferable to choose pseudo-first order conditions to perform the experiments. Each squared derivative of Fig. 7b is weighted by its associated variance given in Fig. 7a to produce the overall variance profile for the fitted rate constant of Fig. 6. So, the species with the lowest associated uncertainty in its initial concentration should be used in excess (here species B). Naturally, these findings go inline with experimental conditions often intuitively followed by kineticists.

4.1.2. 3rd order model ($A+B+C\rightarrow P+C$)

Due to collision theory, elementary reactions of third order are rather unlikely. Nonetheless, empirical mechanisms of this order can be observed and explained by a steady state approximation of a more complex reaction [37]. A typical example taken from homogenous catalysis is a fast pre-equilibrium between a reactant A and a catalyst C to form a steady state complex AC that subsequently reacts with another reactant B to form a product P and to regenerate the catalyst C.

$$A + C \underset{k_{-1}}{\overset{k_1}{\rightleftharpoons}} AC$$
$$AC + B \xrightarrow{k_2} P + C. \tag{13}$$

Application of the steady state approximation on AC under the condition that $k_{-1} \gg k_2 \cdot c_{t,B}$ results in an observed third order reaction of the form

$$A + B + C \xrightarrow{k} P + C \quad \text{with} \quad \frac{dc_{t,P}}{dt} = k \cdot c_{t,A} c_{t,B} c_{t,C} \tag{14}$$

where $k = \frac{k_1 k_2}{k_{-1}}$ is the observed third order rate constant. Under semi-batch conditions, e.g. when catalyst C is dosed, Eq. 14 requires a minor adaptation to take into account dosing and dilution (see Table 1).

The proposed method of error propagation could be successfully applied and validated for semi-batch data simulated by this third order mechanism and subsequent nonlinear optimisations of the rate constant, starting from various initial concentrations and flow rates (for the dosed species C) normally distributed around their true simulated values (Monte-Carlo sampling). The procedure for the Monte-Carlo sampling has been described at the end of Section 3.1. The fitted rate constant and its associated standard deviation ($1.75(2)\pm0.02(2)\cdot10^{-4}$ L^{2}mol^{-2}s^{-1}) predicted by error propagation (Eq. 10) is in perfect agreement with the mean and standard deviation ($1.75(2)\pm0.02(3)\cdot10^{-4}$ L^{2}mol^{-2}s^{-1}) of the 10000 fitted rate constants resulting from the Monte-Carlo sampling. This demonstrates the formal correctness and the accuracy of the developed algorithm to propagate the errors on the initial concentrations and on the flow rate.

It is interesting to note that $\boldsymbol{\sigma}^2_{\mathbf{k},\mathbf{f}}$, the variance due to the dosing rate, contributes the most to the total predicted variance $\boldsymbol{\sigma}^2_{\mathbf{k}}$ and represents the main source of uncertainty (~94%) whereas the variance due to the initial concentrations $\boldsymbol{\sigma}^2_{\mathbf{k},\mathbf{c}_0}$ only accounts for ~6%. The contribution of the variance due to the residuals (0.004%) is basically negligible.

4.2. Experimental data

This section compares the uncertainties in the fitted rate constant based on one experiment only predicted by Eq. 10

with the 'real' one obtained from a collection of 17 independent experiments. The acid catalysed reaction of phenylhydrazine with benzophenone (Fig. 4) was repeatedly studied for this purpose by UV–vis and mid-IR spectroscopy. For batch conditions under acidic excess, it has previously been shown that this reaction follows an overall second order rate law, i.e. first order in both reactants [31]. When the catalyst is dosed (semi-batch conditions), the third order rate law as described in the previous section and in Table 1 (*A*: phenylhydrazine, *B*: benzophenone, *C*: acetic acid, *P*: benzophenone phenylhydrazone) becomes applicable. Note that water, as the by-product, has not been included into the kinetic analysis as it is not required for the rate law and as its spectrum cannot be separated from the pure spectrum of product *P* due to parallel formation.

Fig. 8 compares fitted and measured kinetic absorbance traces at selected wavelengths and wavenumbers for a typical experiment. The sudden change in absorbance after 6 min corresponds to the dosing of acetic acid. Fits were generally good with typical standard deviations in the residuals, $\sigma_r \approx 5 \cdot 10^{-3}$ (UV–vis) and $5 \cdot 10^{-4}$ (mid-IR) explaining more than 99.9% of the total variance for both signals.

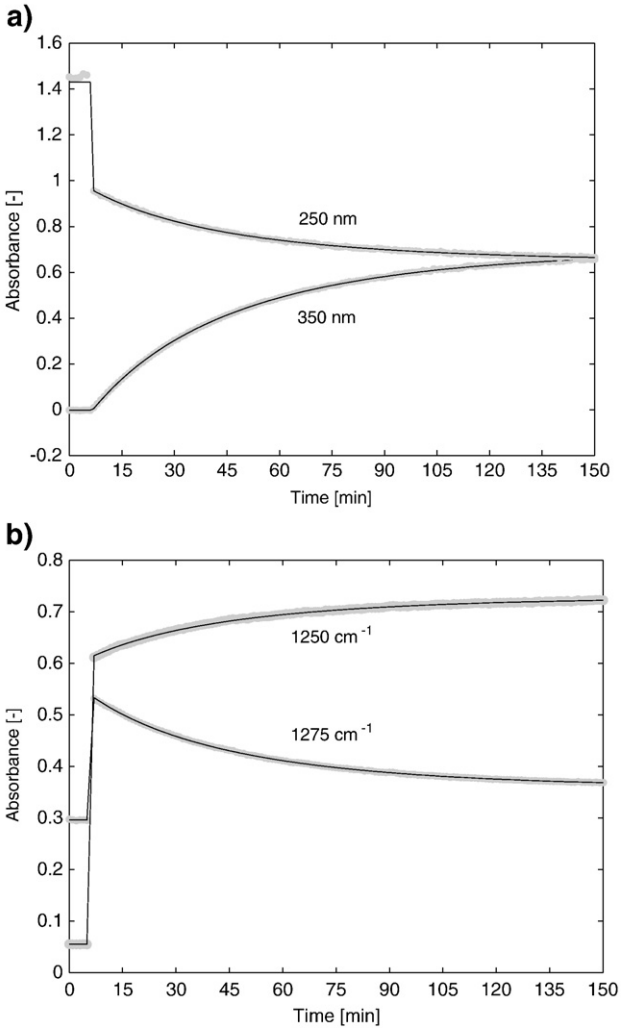

Fig. 8. Comparison of fitted (lines) and measured (circles) absorbance traces in UV–vis (a) and in mid-IR (b). Spectra between 0 and 6 min are recorded before the dosing of the catalyst.

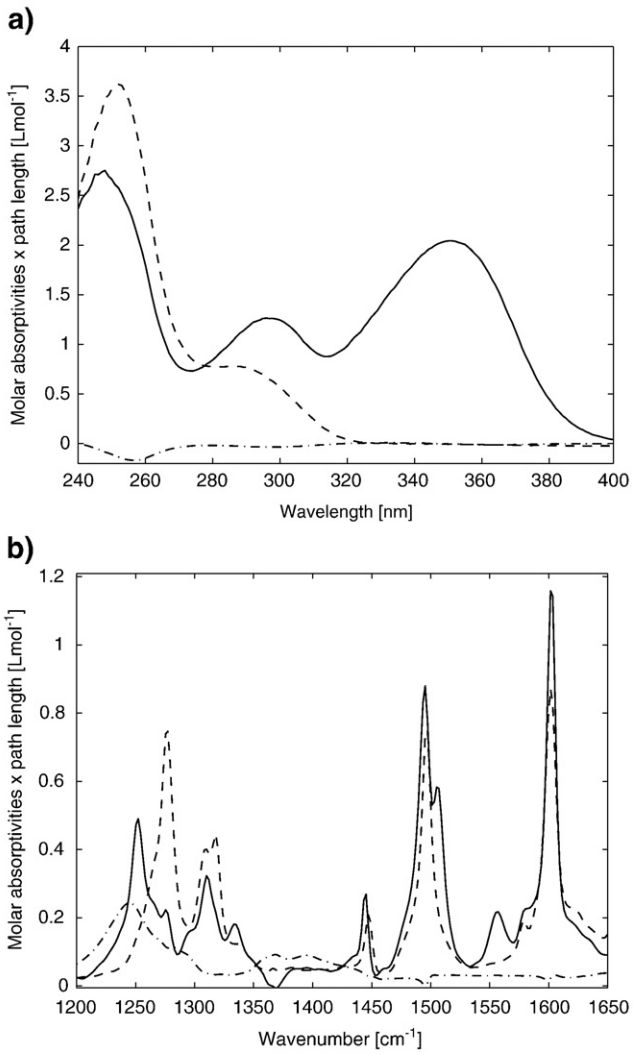

Fig. 9. Fitted pure component spectra for benzophenone phenylhydrazone (solid line), for benzophenone (dashed line), both combined with the spectrum of phenylhydrazine, and resolved pure spectrum of acetic acid (dashed dot line) in UV–vis (a) and mid-IR (b).

Fitted pure component spectra are presented in Fig. 9 for a typical experiment. Note that these spectra are normalised to unity concentrations but not to unity path length as this distance is difficult to estimate for ATR probes. Because of the intrinsic rank deficiency in the concentration profiles for third order rate laws, only linear combinations of the pure component spectra of *A*, *B* and *P* can be obtained [38,39]. Note that the dosed catalyst *C* (acetic acid), although being a low UV–vis absorber ($\lambda_{max} \approx 207$ nm), was also included as an absorbing component in order to allow for unavoidable small baseline shifts during the dosing event (which also affects the mid-IR spectrum of acetic acid). Due to rank deficiency mentioned above, only the pure spectra of acetic acid in UV–vis and mid-IR are resolved and can be compared to independently measured spectra for validation. They were in very good agreement for both UV–vis and mid-IR.

Table 2 summarises all fitted rate constants for the 17 kinetic UV–vis and mid-IR experiments and their associated uncertainties with (Eq. 10) and without (Eq. 8) propagating the errors in the initial concentrations and in the flow rate. An analysis of

Table 2
Fitted third order rate constants and associated uncertainties calculated with and without error propagation for the reaction of benzophenone with phenylhydrazine under semi-batch conditions studied by UV–vis and mid-IR spectroscopy

	UV–vis			mid-IR		
	$\mathbf{k}$[a]	$\boldsymbol{\sigma}_\mathbf{k}$ without error propagation[a,b]	$\boldsymbol{\sigma}_\mathbf{k}$ with error propagation[a,c]	$\mathbf{k}$[a]	$\boldsymbol{\sigma}_\mathbf{k}$ without error propagation[a,b]	$\boldsymbol{\sigma}_\mathbf{k}$ with error propagation[a,c]
# 1	1.75(6)	0.003	0.02(2)	1.74(5)	0.002	0.02(2)
# 2	1.76(6)	0.003	0.02(3)	1.73(0)	0.001	0.02(2)
# 3	1.74(4)	0.003	0.02(2)	1.66(1)	0.003	0.02(2)
# 4	1.75(7)	0.003	0.02(2)	1.72(3)	0.004	0.02(2)
# 5	1.75(2)	0.003	0.02(2)	1.74(8)	0.002	0.02(2)
# 6	1.76(1)	0.003	0.02(2)	1.70(6)	0.003	0.02(1)
# 7	1.78(8)	0.004	0.02(4)	1.76(8)	0.002	0.02(2)
# 8	1.85(2)	0.004	0.02(5)	1.83(5)	0.002	0.02(3)
# 9	1.76(2)	0.004	0.02(3)	1.78(1)	0.004	0.02(2)
# 10	1.76(7)	0.004	0.02(3)	1.78(4)	0.002	0.02(3)
# 11	1.79(2)	0.004	0.02(4)	1.81(2)	0.002	0.02(3)
# 12	1.78(6)	0.004	0.02(4)	1.73(7)	0.004	0.02(2)
# 13	1.76(1)	0.004	0.02(3)	1.75(5)	0.002	0.02(2)
# 14	1.77(7)	0.004	0.02(3)	1.77(4)	0.002	0.02(2)
# 15	1.75(5)	0.004	0.02(3)	1.71(3)	0.003	0.02(2)
# 16	1.71(0)	0.004	0.02(3)	1.62(4)	0.002	0.02(0)
# 17	1.77(8)	0.004	0.02(3)	1.67(2)	0.003	0.02(1)

Numbers in brackets indicate the first insignificant digit.
[a] In $L^2mol^{-2}s^{-1}\times10^{-4}$.
[b] Based on Eq. 8.
[c] Based on Eq. 10.

significance was performed using a z test on the calculated rate constants. It showed that some few calculated rate constants were just close to the significance level of 95% confidence. Removing these values from such a small statistical sample (17 experiments) is arguable and does not affect the subsequent conclusions that can be made on the entire sample. This is why the entire statistical sample was kept intact. Considering the 95% confidence limit, the fitted rate constants and all associated uncertainties in Table 2 are reproducible for both UV–vis and mid-IR. As expected, the uncertainties of the individual rate constants predicted by error propagation are significantly larger than those without error propagation.

As shown in Table 3, the mean rate constants for UV–vis $(1.76(8)\cdot10^{-4}\ L^2mol^{-2}s^{-1})$ and for mid-IR $(1.73(9)\cdot10^{-4}\ L^2mol^{-2}s^{-1})$ are the same within their experimental standard deviation, and are comparable to previously published values reported for the same temperature under batch conditions [31]. Differences could be due to discrepancies in the 'real' nominal temperature, fluctuations thereof, different experimental design (batch versus semi-batch conditions) and a different method for kinetic data analysis (PLS-calibration with subsequent direct fitting of concentration profiles).

For UV–vis spectroscopy, the uncertainty predicted by error propagation $(\boldsymbol{\sigma}_\mathbf{k}=0.02(3)\cdot10^{-4}\ L^2mol^{-2}s^{-1})$ covers more than 80% of the experimental standard deviation over all individually fitted rate constants $(\boldsymbol{\sigma}_\mathbf{k}=0.02(8)\cdot10^{-4}\ L^2mol^{-2}s^{-1})$. This suggests that the approach used to propagate uncertainties in initial concentrations and flow rate is suitable. Possible sources for the remainder could be attributed to effects such as minor instrumental drifts (e.g. in baseline or flow rate) that have not been modelled. Additionally, minor fluctuations in temperature ($\sigma_T^2\approx0.04$ °C) have an impact. Assuming, for example, an activation energy between 50 and 100 kJmoL^{-1} (to our knowledge, the true value is not known), a corresponding contribution incorporated in Eq. 10 due to fluctuations in temperature, $\boldsymbol{\sigma}^2_{\mathbf{k},\mathbf{T}}=\mathrm{diag}((\partial\mathbf{k}/\partial\mathbf{T})^T\sigma_T^2(\partial\mathbf{k}/\partial\mathbf{T}))$ with $\partial\mathbf{k}/\partial\mathbf{T}$ determined from Arrhenius' law, would add between 2% and 8% to the total predicted error $\boldsymbol{\sigma}_\mathbf{k}$. Note that the lack of information in manufacturer's uncertainties in the purity of chemicals did not allow them to be taken into account in the error estimate of the initial concentrations from the sample preparation.

For mid-IR measurements, error propagation $(\boldsymbol{\sigma}_\mathbf{k}=0.02(2)\cdot10^{-4}\ L^2mol^{-2}s^{-1})$ only explains approximately 40% of the experimental uncertainty $(\boldsymbol{\sigma}_\mathbf{k}=0.05(4)\cdot10^{-4}\ L^2mol^{-2}s^{-1})$ in the fitted rate constant. All sources explaining the remaining contributions to the experimental uncertainty listed for UV–vis certainly also apply to mid-IR spectroscopy. One possible reason to explain the lower error predictability observed for mid-IR (40%) compared to UV–vis (80%) could be a generally larger sensitivity to temperature for mid-IR spectroscopy. Another explanation could be a larger deviation from the 'silent' assumption of normally distributed and homoscedastic (i.e. constant standard deviation) noise in the experimental mid-IR absorbance data used for the least squares fitting [40]. This last statement was supported by multiple kinetic fittings at single wavelengths/wavenumbers (with similar absorbance changes) for both UV–vis and mid-IR data leading to a lower wavelength dependency of the residual noise level and of the fitted rate constant for UV–vis. The residual standard deviation of the noise in mid-IR spectroscopy is possibly less constant along the wavenumbers. This could be counteracted by an appropriate weighing of the residuals in Eq. 3 according to a time and wavenumber dependent standard deviation in $\mathbf{Y}$. This method is often called χ^2 (chi square) fitting. The χ^2 fitting will result in another experimental standard deviation in the rate constants (over all 17 experiments) that needs to be compared with their predicted uncertainties for each individual measurement that will also be affected. Thus, the percentage of experimental standard deviation explained by error propagation will change accordingly. A similar effect has already been discussed by Maeder et al [19]. In practice, however, for time resolved multivariate absorbance measurements it can be fairly difficult to reliably determine the individual standard deviations in $\mathbf{Y}$ as the access to the instrument control is generally rather limited by the instrument manufacturer.

The total predicted variance $\boldsymbol{\sigma}^2_\mathbf{k}$ of the rate constant fitted to the UV–vis or mid-IR measurements can be broken down into its individual contributions ($\boldsymbol{\sigma}^2_{\mathbf{k},\mathbf{r}}$, $\boldsymbol{\sigma}^2_{\mathbf{k},\mathbf{c}_0}$, $\boldsymbol{\sigma}^2_{\mathbf{k},\mathbf{f}}$) given in Eq. 10. For both UV–vis and mid-IR, the variance due to the residuals, $\boldsymbol{\sigma}^2_{\mathbf{k},\mathbf{r}}$, has the lowest contribution (~2%), followed by the variance due to the initial concentrations, $\boldsymbol{\sigma}^2_{\mathbf{k},\mathbf{c}_0}$ that explains approximately 6% of the total variance. Clearly the major contribution (~92%) is attributed to $\boldsymbol{\sigma}^2_{\mathbf{k},\mathbf{f}}$, the variance due to the flow rate. This is in good

Table 3
Means of all individually fitted rate constants (columns 2 and 5 of Table 2) compared to their literature values obtained from UV–vis and mid-IR spectroscopy

	UV–vis		Mid-IR	
	$\mathbf{k}$[a]	$\boldsymbol{\sigma}_\mathbf{k}$[a]	$\mathbf{k}$[a]	$\boldsymbol{\sigma}_\mathbf{k}$[a]
Experimental	1.76(8)	0.02(8)	1.73(9)	0.05(4)
Predicted by error propagation	–	0.02(3)	–	0.02(2)
Literature	1.40[b]	[c]	1.51[b]	[c]

Standard deviations associated with columns 2 and 5 of Table 2 are compared to the mean uncertainties predicted by error propagation (columns 4 and 7 of Table 2).
Numbers in brackets indicate the first insignificant digit.
[a] In $L^2mol^{-2}s^{-1}\times10^{-4}$.
[b] For comparison, pseudo-second order rate constants of reference [31] have been recalculated to third order rate constants by division with the excess catalyst concentration given in [31].
[c] Not available.

agreement with the results obtained for simulated data based on the same model discussed in section 4.1.2. Particularly for mid-IR, the 'real' individual contributions might be somewhat different due to possible heteroscedastic noise as outlined in the previous paragraph.

5. Conclusion

The impact of uncertainties in the initial concentrations and dosing rate (batch and/or semi-batch) on the error of rate constants fitted by multivariate nonlinear regression of spectroscopic data has been studied on simulated and experimental data following 2nd and formal 3rd order rate laws. For this, a rigorous approach based on classical error propagation was developed and theoretically validated with simulated data by a 'brute force' Monte-Carlo sampling. Rigorous error propagation required significantly less computation time compared to the Monte Carlo procedure (typically seconds compared to hours on a modern personal computer).

Based on simulated data for a second order rate law under batch conditions, the effect of the uncertainties in the initial reactant concentrations on the predicted error of the fitted rate constant was thoroughly investigated. It was shown that the predicted error in the fitted second order rate constant is minimal when the reactants are mixed in exact stoichiometric amounts, or if the species with the lowest associated uncertainty in its initial concentration is in excess (pseudo-first order conditions). These findings have an immediate application in the optimum experimental design of second order reactions.

The reaction of benzophenone with phenylhydrazine was repeatedly investigated by UV–vis and mid-IR spectroscopy under semi-batch conditions dosing the catalyst (acetic acid). Each measurement was analysed individually using a third order rate law and the standard deviation of each fitted rate constant was predicted by the proposed method of error propagation. For UV–vis, each individual predicted standard deviation covered more than 80% of the experimental standard deviation over all individually fitted rate constants. For mid-IR, the prediction was only capable to explain approximately 40% of the experimental uncertainty in the fitted rate constant. Possible reasons for this lower error predictability could be a larger sensitivity to temperature and/or stronger deviations from an assumed normally distributed and homoscedastic noise for mid-IR compared to UV–vis. Amongst the individual contributions towards the predicted variance in the rate constant, the dosing rate has by far the largest impact (~92%), followed by the initial concentrations (~6%) and the variance due to the residuals (~2%). These individual contributions are in good agreement with the results obtained for data simulated and analysed under similar conditions.

The possibility to reasonably predict the error in the rate constant based on one single multivariate kinetic measurement was demonstrated. The proposed method of error propagation is simple to implement and fast to perform in order to receive a quick estimate of the error in the rate constant and the individual contributions to this error. In practice, however, errors obtained from error propagation should always be compared with the experimental standard deviation obtained from a reasonable number of replicates. One obvious advantage of the rigorous error propagation is its ability to pinpoint the major source of error and to quantify their impact onto the fitted rate constant. In the presented case study, this would clearly be the dosing rate of the pump. Furthermore, Eq. 10 can straightforwardly be extended to also cover other sources of uncertainty provided reasonable error estimates are available and can be propagated; for example, manufacturer's uncertainties in the purity of the chemicals, if available, could be included in Eq. 10 as a fourth term in the error propagation.

6. Notation

As a convention for the notation used in this article, matrices are written in boldface capitals (e.g. **R**), vectors in boldface lowercase (**r**) and scalars in italics (*r*). For indices, lowercase characters are used. Elements of a matrix **R** are denoted as $r_{i,j}$ and elements of a vector **r** as r_i.

Symbol	Dimension	Units	Description
$\mathbf{Y}$	$(nt\times nw)$		Spectroscopic measurements
$\mathbf{C}$	$(nt\times nc)$	$\mathrm{molL^{-1}}$	Concentration profiles
$\mathbf{A}$	$(nc\times nw)$	$\mathrm{LmoL^{-1}}$	Pure component spectra
$\mathbf{R}$	$(nt\times nw)$		Residuals
$\mathbf{r}$	$(nt\cdot nw\times 1)$		Vectorised residuals
$\mathbf{J}$	$(nt\cdot nw\times nk)$		Jacobian
$\mathbf{H}$	$(nk\times nk)$		Hessian matrix
$\mathbf{k}$	$(1\times nk)$	a)	Rate constants
$\mathbf{c_0}$	$(1\times nc)$	$\mathrm{molL^{-1}}$	Initial concentrations
$\mathbf{f}$	$(1\times nf)$	$\mathrm{Ls^{-1}}$	Dosing (flow) rates for the different dosing steps
$\mathbf{k_{opt}}$	$(1\times nk)$	a)	Optimised rate constants
$\mathbf{\Delta k}$	$(1\times nk)$	a)	Shift vector applied on **k**
$\boldsymbol{\sigma}^2_{\mathbf{k}}$	$(1\times nk)$	b)	Variances in the rate constants
$\boldsymbol{\sigma}^2_{\mathbf{c}_0}$	$(1\times nc)$	$\mathrm{mol^2L^{-2}}$	Variances in the initial concentrations
$\sigma^2_{\mathbf{f}}$	$(1\times nf)$	$\mathrm{L^2s^{-2}}$	Variances in the dosing (flow) rates
$\boldsymbol{\sigma}^2_{\mathbf{k,r}}$	$(1\times nk)$	b)	Variances of **k** due to the residuals
$\boldsymbol{\sigma}^2_{\mathbf{k},\mathbf{c}_0}$	$(1\times nk)$	b)	Variances of **k** due to the initial concentrations
$\boldsymbol{\sigma}^2_{\mathbf{k,f}}$	$(1\times nk)$	b)	Variances of **k** due to the dosing rates
diag( )			Operator extracting a vector of diagonal elements from a matrix argument
DIAG( )			Operator generating a diagonal matrix from a vector argument
nt	Scalar		Number of reaction times
nw	Scalar		Number of wavelengths/wavenumbers
nc	Scalar		Number of absorbing species
nk	Scalar		Number of rate constants
nf	Scalar		Number of different dosing steps
V_t	Scalar	L	Volume at time t
$d_{i,i}$	Scalar		i-th diagonal element of the inverted Hessian $\mathbf{H}^{-1}$
σ^2_r	Scalar		Variance of the residuals **R** or **r**
σ^2_y	Scalar		Variance of the measurement **Y**
ssq	Scalar		Sum of squared residuals
A, B, C, P, S			Chemical species A, B, C, P and S
$c_{t,A}$, $c_{t,B}$, $c_{t,C}$, $c_{t,P}$, $c_{t,S}$		$\mathrm{molL^{-1}}$	Concentrations of species A, B, C, P and S at time t
$c_{\mathrm{dos},C}$		$\mathrm{molL^{-1}}$	Dosed concentration of species C
$c_{0,A}$, $c_{0,B}$	Scalar	$\mathrm{molL^{-1}}$	Initial concentration of species A, B
$c_{\mathrm{tot}}=c_{0,A}+c_{0,B}$	Scalar	$\mathrm{molL^{-1}}$	Sum of the initial concentrations of species A and B
$c^{\mathrm{flask}}_{0,A}$, $c^{\mathrm{flask}}_{0,B}$	Scalar	$\mathrm{molL^{-1}}$	Initial concentration of species A, B in the flask
V^{flask}_A, V^{flask}_B	Scalar	L	Volume of the flask containing species A, B
V^{pip1}_A, V^{pip1}_B	Scalar	L	Volume of species A, B delivered by a 10 mL pipette
V^{pip2}_A, V^{pip2}_B	Scalar	L	Volume of species A, B delivered by a 5 mL pipette
V_{tot}	Scalar	L	$V^{\mathrm{pip1}}_A+V^{\mathrm{pip1}}_B+V^{\mathrm{pip2}}_A$, V^{pip2}_B
m_A, m_B	Scalar	g	Weighed mass of A, B
M_A, M_B	Scalar	$\mathrm{gmoL^{-1}}$	Molecular mass of A, B
X	Scalar		Conversion
t_X	Scalar	s	Time required to reach a conversion X
δk_i, $\delta c_{0,n}$, δf_{m}	Scalar		Finite difference applied to k_{i}, $c_{0,\mathrm{n}}$ and f_{m} for numerical differentiation

a) Units depend on the order of the rate law ($[\mathrm{molL^{-1}s^{-1}}]$ for 0th, $[\mathrm{s^{-1}}]$ for 1st, $[\mathrm{LmoL^{-1}s^{-1}}]$ for 2nd and $[\mathrm{L^2mol^{-2}s^{-1}}]$ for 3rd order rate constants).
b) Units depend on the order of the rate law ($[\mathrm{mol^2L^{-2}s^{-2}}]$ for 0th, $[\mathrm{s^{-2}}]$ for 1st, $[\mathrm{L^2mol^{-2}s^{-2}}]$ for 2nd and $[\mathrm{L^4mol^{-4}s^{-2}}]$ for 3rd order rate constants).

Appendix A

1. Error estimation in the initial concentrations due to sample preparation

Errors in the sample preparation (as described in 3.2.1) for the reactants phenylhydrazine (A) and benzophenone (B) were determined by propagating the following uncertainties of the equipment:

1. Weighing: $\sigma_{m_A}=\sigma_{m_B}=0.0001$ g
2. Filling the volumetric 50 mL flasks: $\sigma_{V_A^{\text{flask}}}=\sigma_{V_B^{\text{flask}}}=0.06$ mL
3. Pipetting (pip1: 10 mL, pip2: 5 mL): $\sigma_{V_A^{\text{pip1}}}=\sigma_{V_B^{\text{pip1}}}=\sigma_{V_A^{\text{pip2}}}=\sigma_{V_B^{\text{pip2}}}=0.04$ mL

For description of the variables we refer to the list of symbols. The initial concentrations ($c_{0,A}$ and $c_{0,B}$) in the reactor were calculated according to:

$$c_{0,A}=\frac{c_{0,A}^{\text{flask}}\cdot\left(V_A^{\text{pip1}}+V_A^{\text{pip2}}\right)}{V_{\text{tot}}}\quad\text{and}\quad c_{0,B}=\frac{c_{0,B}^{\text{flask}}\cdot\left(V_B^{\text{pip1}}+V_B^{\text{pip2}}\right)}{V_{tot}}$$

$$\text{with}\quad c_{0,A}^{\text{flask}}=m_A/\left(M_A\cdot V_A^{\text{flask}}\right),\quad c_{0,B}^{\text{flask}}=m_B/\left(M_B\cdot V_B^{\text{flask}}\right)\quad\text{and}\quad V_{\text{tot}}=V_A^{\text{pip1}}+V_A^{\text{pip2}}+V_B^{\text{pip1}}+V_B^{\text{pip2}}$$

Rigorous error propagation is performed via the total derivatives of $c_{0,A}$ and $c_{0,B}$:

$$\sigma_{c_{0,A}}^2=\left(\frac{\partial c_{0,A}}{\partial m_A}\right)^2\cdot\sigma_{m_A}^2+\left(\frac{\partial c_{0,A}}{\partial V_A^{\text{flask}}}\right)^2\cdot\sigma_{V_A^{\text{flask}}}^2+\left(\frac{\partial c_{0,A}}{\partial V_A^{\text{pip1}}}\right)^2\cdot\sigma_{V_A^{\text{pip1}}}^2+\left(\frac{\partial c_{0,A}}{\partial V_A^{\text{pip2}}}\right)^2\cdot\sigma_{V_A^{\text{pip2}}}^2+\left(\frac{\partial c_{0,A}}{\partial V_B^{\text{pip1}}}\right)^2\cdot\sigma_{V_B^{\text{pip1}}}^2+\left(\frac{\partial c_{0,A}}{\partial V_B^{\text{pip2}}}\right)^2\cdot\sigma_{V_B^{\text{pip2}}}^2$$

$$\sigma_{c_{0,B}}^2=\left(\frac{\partial c_{0,B}}{\partial m_B}\right)^2\cdot\sigma_{m_B}^2+\left(\frac{\partial c_{0,B}}{\partial V_B^{\text{flask}}}\right)^2\cdot\sigma_{V_B^{\text{flask}}}^2+\left(\frac{\partial c_{0,B}}{\partial V_B^{\text{pip1}}}\right)^2\cdot\sigma_{V_B^{\text{pip1}}}^2+\left(\frac{\partial c_{0,B}}{\partial V_B^{\text{pip2}}}\right)^2\cdot\sigma_{V_B^{\text{pip2}}}^2+\left(\frac{\partial c_{0,B}}{\partial V_A^{\text{pip1}}}\right)^2\cdot\sigma_{V_A^{\text{pip1}}}^2+\left(\frac{\partial c_{0,B}}{\partial V_A^{\text{pip2}}}\right)^2\cdot\sigma_{V_A^{\text{pip2}}}^2$$

The variances of A and B have therefore the following expression:

$$\sigma_{c_{0,A}}^2=\left(\left(\frac{\sigma_{m_A}}{m_A}\right)^2+\left(\frac{\sigma_{V_A^{\text{flask}}}}{V_A^{\text{flask}}}\right)^2+\left(\frac{1}{V_A^{\text{pip1}}+V_A^{\text{pip2}}}-\frac{1}{V_{tot}}\right)^2\cdot\left(\sigma_{V_A^{\text{pip1}}}^2+\sigma_{V_A^{\text{pip2}}}^2\right)+\left(\frac{1}{V_{tot}}\right)^2\cdot\left(\sigma_{V_B^{\text{pip1}}}^2+\sigma_{V_B^{\text{pip2}}}^2\right)\right)c_{0,A}^2$$

$$\sigma_{c_{0,B}}^2=\left(\left(\frac{\sigma_{m_B}}{m_B}\right)^2+\left(\frac{\sigma_{V_B^{\text{flask}}}}{V_B^{\text{flask}}}\right)^2+\left(\frac{1}{V_B^{\text{pip1}}+V_B^{\text{pip2}}}-\frac{1}{V_{tot}}\right)^2\cdot\left(\sigma_{V_B^{\text{pip1}}}^2+\sigma_{V_B^{\text{pip2}}}^2\right)+\left(\frac{1}{V_{\text{tot}}}\right)^2\cdot\left(\sigma_{V_A^{\text{pip1}}}^2+\sigma_{V_A^{\text{pip2}}}^2\right)\right)c_{0,B}^2$$

2. Analytical derivatives of a second order rate constant with respect to the initial concentrations

The system of ODEs describing a second order rate law can be integrated explicitly [36] in order to obtain the concentrations of A and B at any time t_X, i.e. the time required to reach conversion X. Subsequent rearrangement for the rate constant $\mathbf{k}$ leads to:

$$\mathbf{k}=\frac{1}{t_X\left(c_{0,B}-c_{0,A}\right)}\cdot\ln\left(\frac{c_{0,B}-c_{0,A}X}{c_{0,B}(1-X)}\right)\qquad\text{for } c_{0,A}<c_{0,B}$$

$$\mathbf{k}=\frac{2X}{t_X\left(c_{0,A}+c_{0,B}\right)\cdot(1-X)}\qquad\text{for } c_{0,A}=c_{0,B}$$

$$\mathbf{k}=\frac{1}{t_X\left(c_{0,B}-c_{0,A}\right)}\cdot\ln\left(\frac{c_{0,A}(1-X)}{c_{0,A}-c_{0,B}X}\right)\qquad\text{for } c_{0,A}>c_{0,B}$$

The analytical partial derivatives of $\mathbf{k}$ with respect to $c_{0,A}$ and $c_{0,B}$ are given by the following expressions:

$$\left(\frac{\partial\mathbf{k}}{\partial c_{0,A}}\right)=\frac{\mathbf{k}}{\left(c_{0,B}-c_{0,A}\right)}+\frac{1}{t_X}\cdot\frac{X}{\left(c_{0,A}X-c_{0,B}\right)\left(c_{0,B}-c_{0,A}\right)}$$
$$\left(\frac{\partial\mathbf{k}}{\partial c_{0,B}}\right)=-\frac{\mathbf{k}}{\left(c_{0,B}-c_{0,A}\right)}-\frac{1}{t_X}\cdot\frac{c_{0,A}}{c_{0,B}}\cdot\frac{X}{\left(c_{0,A}X-c_{0,B}\right)\left(c_{0,B}-c_{0,A}\right)}\qquad\text{for } c_{0,A}<c_{0,B}$$

$$\left(\frac{\partial\mathbf{k}}{\partial c_{0,A}}\right)=\left(\frac{\partial\mathbf{k}}{\partial c_{0,B}}\right)=-\frac{1}{t_X}\cdot\frac{2X}{(1-X)}\cdot\frac{1}{\left(c_{0,A}+c_{0,B}\right)^2}=-\frac{\mathbf{k}}{\left(c_{0,A}+c_{0,B}\right)}=-\frac{\mathbf{k}}{c_{tot}}\qquad\text{for } c_{0,A}=c_{0,B}$$

$$\left(\frac{\partial\mathbf{k}}{\partial c_{0,A}}\right)=\frac{\mathbf{k}}{\left(c_{0,B}-c_{0,A}\right)}+\frac{1}{t_X}\cdot\frac{c_{0,B}}{c_{0,A}}\cdot\frac{X}{\left(c_{0,B}X-c_{0,A}\right)\left(c_{0,B}-c_{0,A}\right)}$$
$$\left(\frac{\partial\mathbf{k}}{\partial c_{0,B}}\right)=-\frac{\mathbf{k}}{\left(c_{0,B}-c_{0,A}\right)}-\frac{1}{t_X}\cdot\frac{X}{\left(c_{0,B}X-c_{0,A}\right)\left(c_{0,B}-c_{0,A}\right)}\qquad\text{for } c_{0,A}>c_{0,B}$$

Towards strong pseudo-first order conditions in B ($c_{0,A}\ll c_{0,B}$):

$$\lim_{c_{0,A}\to 0}\left(\frac{\partial\mathbf{k}}{\partial c_{0,B}}\right)=\lim_{c_{0,A}\to 0}-\frac{\mathbf{k}}{\left(c_{0,B}-c_{0,A}\right)}-c_{0,A}\left(\frac{1}{t_X}\cdot\frac{1}{c_{0,B}}\cdot\frac{X}{\left(c_{0,A}X-c_{0,B}\right)\left(c_{0,B}-c_{0,A}\right)}\right)=-\frac{\mathbf{k}}{c_{0,B}}=-\frac{\mathbf{k}}{c_{\text{tot}}}$$

Towards strong pseudo-first order conditions in A ($c_{0,A} \gg c_{0,B}$):

$$\lim_{c_{0,B}\to 0}\left(\frac{\partial \mathbf{k}}{\partial c_{0,A}}\right) = \lim_{c_{0,B}\to 0}\frac{\mathbf{k}}{(c_{0,B}-c_{0,A})} + c_{0,B}\left(\frac{1}{t_X}\cdot\frac{1}{c_{0,A}}\cdot\frac{X}{(c_{0,B}X-c_{0,A})(c_{0,B}-c_{0,A})}\right) = -\frac{\mathbf{k}}{c_{0,A}} = -\frac{\mathbf{k}}{c_{\mathrm{tot}}}$$

References

[1] B. Ma, P.J. Gemperline, E. Cash, M. Bosserman, E. Comas, J. Chemom. 17 (2003) 470–479.
[2] G. Puxty, U. Fischer, M. Jecklin, K. Hungerbühler, Chimia 60 (2006) 605–610.
[3] A.E. Rubin, S. Tummala, D.A. Both, C.C. Wang, E.J. Delaney, Chemical Reviews 106 (2006) 2794–2810.
[4] J. Workman, M. Koch, D. Veltkamp, Anal. Chem. 79 (2007) 4345–4363.
[5] E.R. Malinowski, Factor Analysis in Chemistry, Third Edition John Wiley & Sons, Inc., New York, USA, 2002.
[6] M. Maeder, Anal. Chem. 59 (1987) 527–530.
[7] J. Saurina, S. Hernandez-Cassou, R. Tauler, A. Izquierdo-Ridorsa, J. Chemom. 12 (1998) 183–203.
[8] J. Jaumot, R. Gargallo, R. Tauler, J. Chemom. 18 (2004) 327–340.
[9] A. de Juan, M. Maeder, M. Martinez, R. Tauler, Chemom. Intell. Lab. Syst. 54 (2000) 123–141.
[10] E. Bezemer, S.C. Rutan, Chemom. Intell. Lab. Syst. 59 (2001) 19–31.
[11] G.M. Escandar, N.K.M. Faber, H.C. Goicoechea, A.M. de la Pena, A.C. Olivieri, R.J. Poppi, Trac-Trends Anal. Chem. 26 (2007) 752–765.
[12] P. Geladi, B.R. Kowalski, Anal. Chim. Acta 185 (1986) 1–17.
[13] I.M. Galvan, J.M. Zaldivar, H. Hernandez, E. Molga, Comput. Chem. Eng. 20 (1996) 1451–1465.
[14] M. Maeder, A.D. Zuberbühler, Anal. Chem. 62 (1990) 2220–2224.
[15] E. Furusjö, L.G. Danielsson, Anal. Chim. Acta 373 (1998) 83–94.
[16] S. Bijlsma, D.J. Louwerse, A.K. Smilde, AIChE J. 44 (1998) 2713–2723.
[17] G. Puxty, M. Maeder, K. Hungerbühler, Chemom. Intell. Lab. Syst. 81 (2006) 149–164.
[18] M. Maeder, Y.M. Neuhold, , Chapter 7, in: P. Gemperline (Ed.), Practical Guide to Chemometrics, Taylor and Francis, Boca Raton, USA, 2006.
[19] M. Maeder, Y.M. Neuhold, Practical Data Analysis in Chemistry, Elsevier, Amsterdam, NL, 2007.
[20] P. Gemperline, G. Puxty, M. Maeder, D. Walker, F. Tarczynski, M. Bosserman, Anal. Chem. 76 (2004) 2575–2582.
[21] T. Kourti, Crit. Rev. Anal. Chem. 36 (2006) 257–278.
[22] K.Q. Levenberg, Appl. Math. 2 (1949) 164–168.
[23] D.W. Marquardt, J. Soc. Ind. Appl. Math. 11 (1963) 431–441.
[24] W.H. Press, W.T. Vetterling, S.A. Teukolsky, B.P. Flannery, Numerical Recipes in C++ - The art of Scientific Computing, Second Edition Cambridge University Press, New York, USA, 2005.
[25] P.R. Bevington, D.K. Robinson, Data reduction and error analysis for the physical sciences, Mcgraw-Hill, New York, USA, 2003.
[26] E. Furusjö, L.G. Danielsson, J. Chemom. 14 (2000) 483–499.
[27] V.M. Taavitsainen, H. Haario, J. Chemom. 15 (2001) 215–239.
[28] S. Bijlsma, H.F.M. Boelens, H.C.J. Hoefsloot, A.K. Smilde, J. Chemom. 16 (2002) 28–40.
[29] A.R. Carvalho, R.G. Brereton, T.J. Thurston, R.E.A. Escott, Chemom. Intell. Lab. Syst. 71 (2004) 47–60.
[30] V.M. Taavitsainen, H. Haario, M. Laine, J. Chemom. 17 (2003) 140–150.
[31] A.R. de Carvalho, M.D. Sanchez, J. Wattoom, R.G. Brereton, Talanta 68 (2006) 1190–1200.
[32] R. Dyson, M. Maeder, G. Puxty, Y.M. Neuhold, Inorg. React. Mech. 5 (2003) 39–46.
[33] Matlab 7.5.0 (R2007b), The Mathworks, Natick, MA, USA, 2007 http://www.mathworks.com.
[34] J.F. Zhang, IEEE Trans. Rel. 55 (2006) 169–181.
[35] F. Visentin, S.I. Gianoli, A. Zogg, O.M. Kut, K. Hungerbühler, Org. Proc. Res. Dev. 8 (2004) 725–737.
[36] K.J. Laidler, J.H. Meiser, B.C. Sanctuary, Physical Chemistry, Houghton Mifflin, Boston, USA, 2003.
[37] J.H. Espenson, Chemical kinetics and reaction mechanisms, Mcgraw-Hill, New York, USA, 1995.
[38] R.N. Cochran, F.H. Horne, Anal. Chem. 49 (1977) 846–853.
[39] M. Amrhein, B. Srinivasan, D. Bonvin, M.M. Schumacher, Chemom. Intell. Lab. Syst. 33 (1996) 17–33.
[40] J. Tellinghuisen, Appl. Spectrosc. 54 (2000) 1208–1213.